Universal Dimensionless Framework for Morphological Computing in Hyperelastic Stick-Slip Soft Robotic Locomotion

Anih Chibueze Victor
Department of Mechatronics Engineering, University of Nigeria, Nsukka
victor.anih.251139@unn.edu.ng

Abstract

Purpose: Soft pneumatic actuators exhibit immense potential as computational reservoirs due to their hyperelasticity and slow fluidic response. However, empirical data-driven learning often obscures the universal scaling laws and physical limits of the underlying mechanics. This paper aims to establish a foundational, physics-based model for unanchored soft stick-slip robots to identify optimal computational regimes and expose the limitations of continuous sparse regression.
Methods: We derive a dimensionally consistent, two-mass hybrid analytical model that reduces a soft stick-slip crawler to its fundamental state variables. The model integrates true Coulomb stick-slip friction to capture macroscopic translation and phase transitions without deleting internal restoring forces. Furthermore, we investigate the application of sparse regression (SINDy), including standard and custom non-smooth basis libraries, to recover the governing dynamics.
Results: By identifying the fundamental dimensionless groups, we map the system's parameter space and demonstrate that the physical reservoir achieves its maximum Memory Capacity exactly at the boundary between stability and chaos. The sparse regression evaluation reveals that standard continuous empirical discovery fails to recover the discontinuous acceleration spikes generated by the mechanical diode effect, defining a Kinetic Stiffness Limit.
Conclusion: The failure of continuous regression algorithms on stick-slip discontinuities highlights a severe vulnerability in off-the-shelf empirical modeling. This underscores the necessity of first-principles derivations for hybrid dynamical systems in soft robotics, ensuring that contact-driven phase transitions are mathematically preserved.

Keywords: Nonlinear Dynamics, Morphological Computing, Stick-Slip Friction, Reservoir Computing, System Identification.

1 Introduction

1.1 Biological Inspiration and Morphological Computation

In traditional rigid robotics, the paradigm of control is strictly compartmentalized: sensors measure the environment, a centralized microcontroller computes a control policy, and actuators execute the resulting commands. However, biological systems operate fundamentally differently. For example, an octopus does not rely on a centralized brain to micromanage every kinematic degree of freedom in its appendages. Instead, each soft arm can react intelligently to local stimuli, execute complex grasping motions, and navigate obstacles seamlessly [1]. This distributed intelligence is facilitated by the physical properties of the tissues themselves—their compliance, continuous deformation, and fluidic dynamics naturally process mechanical information.

This paradigm, where the physical body itself assumes a portion of the computational burden, is known as morphological computing. When engineered into soft pneumatic actuators, elastomeric materials possess continuous degrees of freedom, nonlinear stiffness, and material memory. Consequently, they naturally map low-dimensional input signals into a high-dimensional state space. This behavior is mathematically analogous to Reservoir Computing (RC), traditionally implemented using recurrent neural networks [2, 3]. By treating the soft body as a physical reservoir, complex temporal processing tasks can be offloaded to the mechanical structure.

1.2 Challenges in Analytical and Empirical Modeling

The field currently relies heavily on either computationally expensive finite-element simulations or black-box empirical models. Methods such as SINDy (Sparse Identification of Nonlinear Dynamics) [4] excel at finding governing equations from data in smooth, continuous applications. However, unanchored soft locomotion relies on fluid power and stick-slip friction, which create sharp, discontinuous acceleration spikes. Continuous polynomial basis functions cannot adequately capture these contact-driven events without filtering out high frequencies, thereby obscuring the actual physics.

2 Methods: Analytical First-Principles Framework

2.1 The Two-Mass Hybrid System

We model the soft pneumatic actuator as a hyperelastic body of unpressurized rest length L_0, internal cross-sectional area A_0, and linear stiffness k_1. To capture the physics of unanchored forward locomotion without artificially removing the restoring springs, the system is modeled as a two-mass hybrid dynamical system consisting of a payload mass (m_p) and a frictional foot mass (m_f).

Let $X_p(t)$ and $X_f(t)$ represent the global absolute positions. The internal deformation is defined as $z(t) = X_p(t) - X_f(t) - L_0$. For a neo-Hookean hyperelastic material, the elastic potential energy yields a restoring force featuring both linear and cubic stiffness parameters:

$F_{\text{elastic}} = k_1 z + k_3 z^3$. Accounting for radial Poisson expansion during elongation, the internal active fluidic force scales as $P(t)A_0(1 + \alpha z)$.

The net internal active and restoring force (F_{int}) generated by the actuator, incorporating structural viscous damping $b\dot{z}$, is:

$$F_{\text{int}} = P(t)A_0(1 + \alpha z) - k_1 z - k_3 z^3 - b\dot{z} \tag{1}$$

2.2 Thermodynamic Pressure Dynamics

The internal pressure follows an isothermal lumped-capacitance model with a fluidic time constant τ. For a binary valve input $u(t) \in \{0, 1\}$ connected to a supply $P_{\max}$:

$$\dot{P}(t) = \frac{-P(t) + P_{\max} u(t)}{\tau} \tag{2}$$

2.3 Dimensionless Scaling Parameters

The characteristic length is defined by the static deformation under maximum pneumatic pressure: $z_c = \frac{P_{\max} A_0}{k_1}$. The characteristic time is the natural period: $t_c = \sqrt{m_{\text{eff}}/k_1}$, where $m_{\text{eff}} = m_p + m_f$. Defining $\tilde{z} = z/z_c$, $\tilde{t} = t/t_c$, and $\tilde{P} = P/P_{\max}$ yields four fundamental dimensionless groups:

$$\Pi_1 = \frac{k_3 z_c^2}{k_1} \qquad \text{(Duffing nonlinearity)} \tag{3}$$

$$\Pi_2 = \frac{b}{2\sqrt{m_{\text{eff}} k_1}} \qquad \text{(Viscous damping ratio)} \tag{4}$$

$$\Pi_4 = \frac{\tau}{t_c} \qquad \text{(Deborah fluid number)} \tag{5}$$

$$\Pi_5 = \alpha z_c \qquad \text{(Radial coupling factor)} \tag{6}$$

2.4 Transition to Unanchored Stick-Slip Locomotion

Forward locomotion relies on a mechanical diode effect governed by true Coulomb friction. The ground applies static friction ($\mu_s m_f g$) and kinetic friction ($\mu_k m_f g$).

1) Stick Phase: During pneumatic charging, if $|-F_{\text{int}}| \leq \mu_s m_f g$, the foot is anchored ($\dot{X}_f = 0$):

$$m_p \ddot{X}_p = F_{\text{int}} \tag{7}$$

2) Slip Phase: When the spring violently contracts and $-F_{\text{int}} > \mu_s m_f g$, the foot breaks static contact:

$$m_p \ddot{X}_p = F_{\text{int}} \tag{8}$$

$$m_f \ddot{X}_f = -F_{\text{int}} - \mu_k m_f g \tag{9}$$

The slip phase terminates when $\dot{X}_f \leq 0$.

3 Methods: Reservoir Computing and Stability Metrics

3.1 State as a Physical Reservoir

The soft body operates as a physical reservoir. By extracting the state vector $\mathbf{R}(t) = [z(t), \dot{z}(t), P(t)]^T$, a linear combination approximates a target output $y(t)$:

$$\hat{y}(t) = \mathbf{W}_{\text{out}}\mathbf{R}(t) \tag{10}$$

The optimal readout weights $\mathbf{W}_{\text{out}}$ are computed using ridge regression:

$$\mathbf{W}_{\text{out}} = \mathbf{Y}\mathbf{R}^T(\mathbf{R}\mathbf{R}^T + \lambda\mathbf{I})^{-1} \tag{11}$$

3.2 Performance Metrics and Lyapunov Exponents

Memory Capacity (MC) for a temporal delay d is defined as:

$$\text{MC}_d = \frac{\text{Cov}^2(\hat{u}_d(t), u(t - d\Delta t))}{\text{Var}(\hat{u}_d(t)) \cdot \text{Var}(u(t - d\Delta t))} \tag{12}$$

To map dynamical stability, the Largest Lyapunov Exponent (LLE) measures the exponential divergence rate of infinitesimally close trajectories [5]:

$$\lambda_{\max} = \lim_{t\to\infty} \lim_{|\delta\mathbf{X}_0|\to 0} \frac{1}{t} \ln \frac{|\delta\mathbf{X}(t)|}{|\delta\mathbf{X}_0|} \tag{13}$$

4 Results

4.1 Macroscopic Translation and Numerical Verification

Figure 1 illustrates the macroscopic translation of the analytical model. The 1-DOF assumption was numerically verified against a high-fidelity multibody physical twin (Simscape), achieving an NMSE of 0.0028.

4.2 Energy-Information Landscape and Edge of Chaos

Figure 2 presents the total mechanical work plotted against the Duffing parameter Π_1, mapped by Memory Capacity. Peak computational performance is strictly localized to moderate mechanical work levels.

Figure 3 maps the Largest Lyapunov Exponent across the Π_1 versus Π_4 parameter space. The boundary where $\lambda_{\max} \approx 0$ delineates the edge of chaos, precisely where the physical reservoir achieves its maximum Memory Capacity.

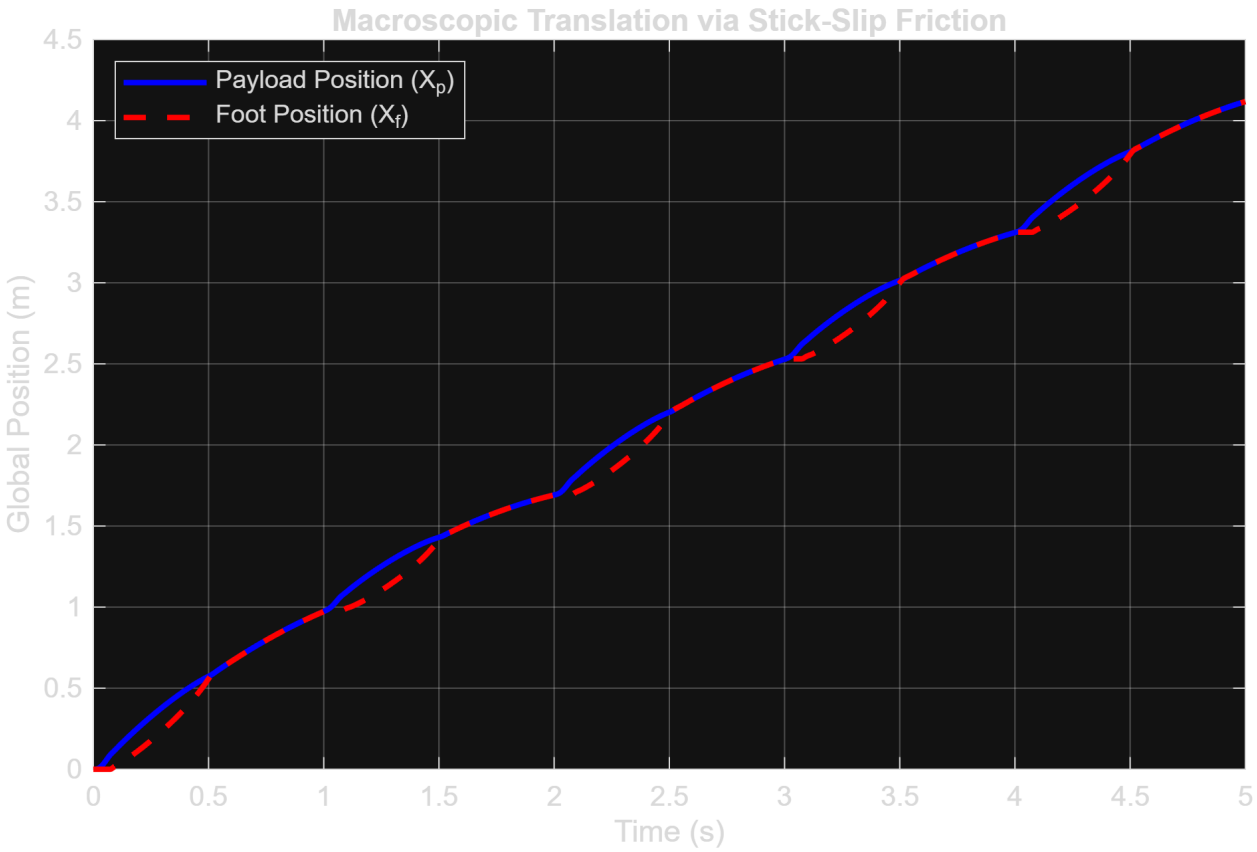

Figure 1: True Coulomb stick-slip locomotion. Blue solid: payload position $X_p(t)$. Red dashed: foot position $X_f(t)$.

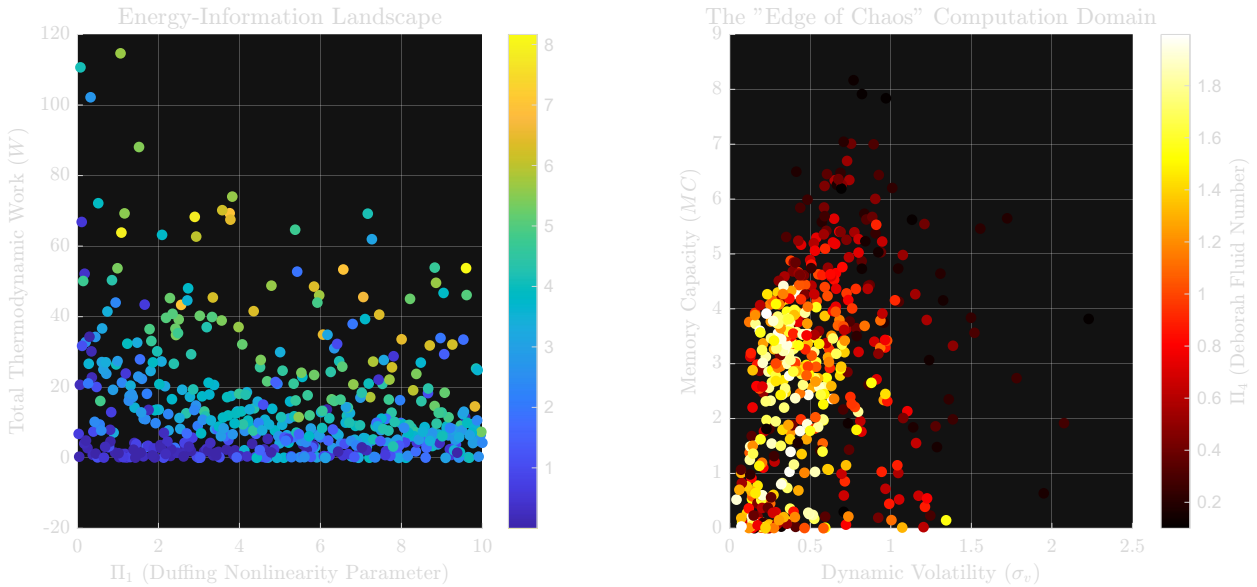

Figure 2: Energy-Information Landscape: total mechanical work vs. Π_1, color-mapped by Memory Capacity.

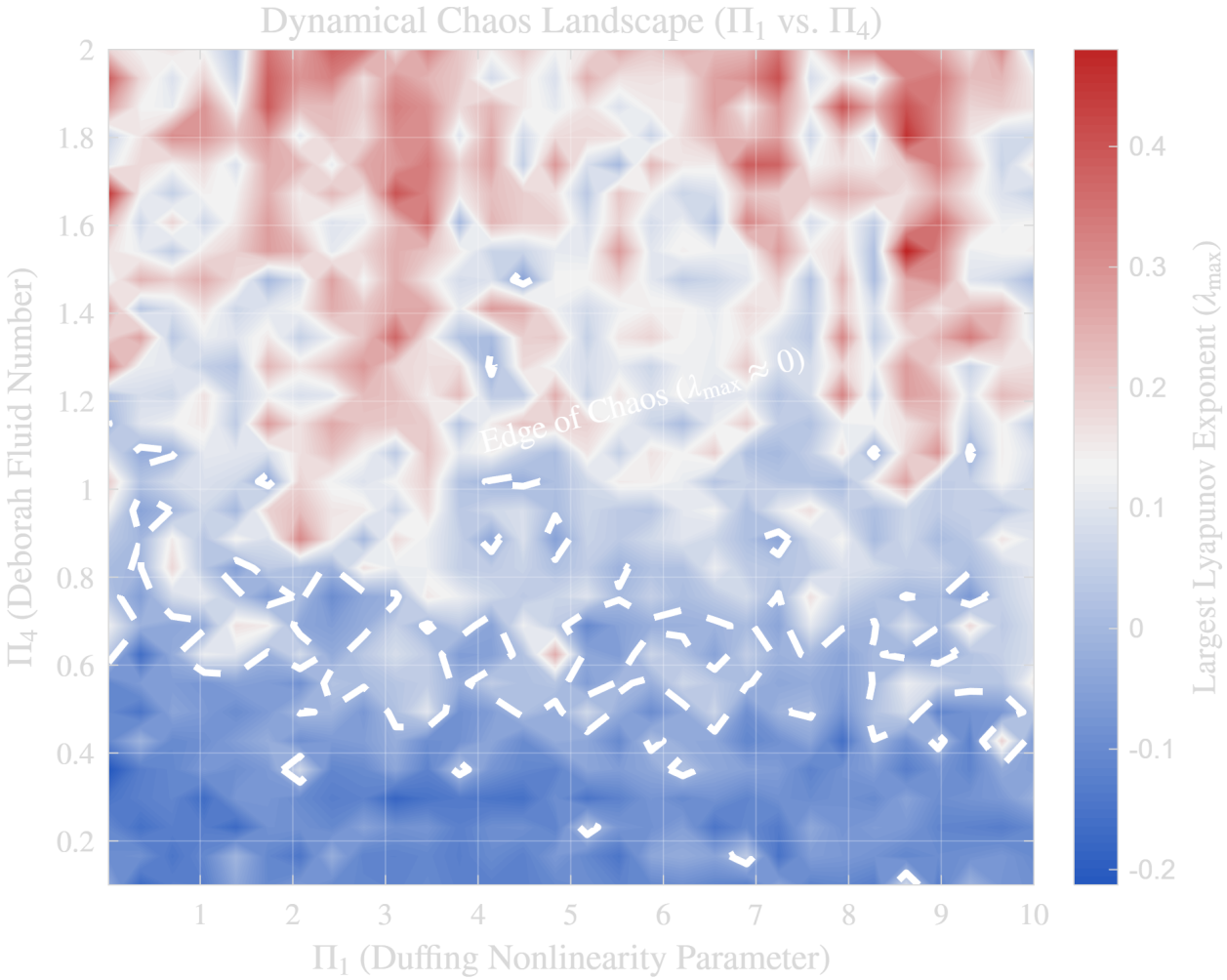

Figure 3: Largest Lyapunov Exponent $\lambda_{\max}$ vs. Π_1 and Π_4. White dashed line marks $\lambda_{\max} = 0$.

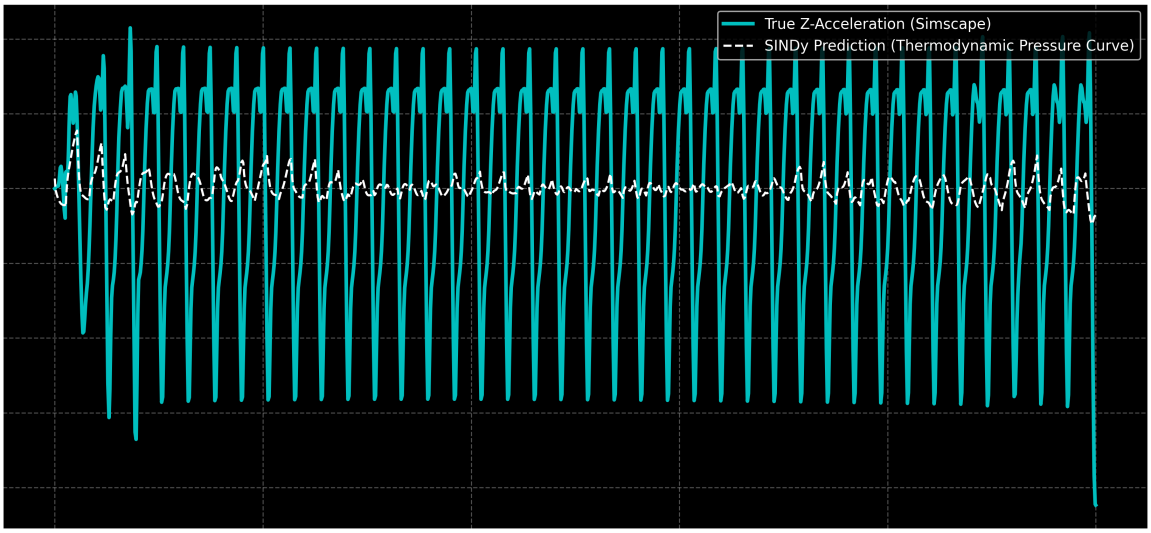

Figure 4: Failure of standard SINDy. The polynomial basis cannot represent the sharp acceleration spikes generated by stick-slip transitions.

4.3 SINDy and the Kinetic Stiffness Limit

Standard data-driven sparse regression (SINDy) utilizing polynomial basis libraries struggles to capture the high-frequency acceleration shocks characteristic of stick-slip locomotion (Figure 4).

Furthermore, empirical algorithms erroneously identify quadratic terms due to the Pre-Strain Artifact. When subjected to a static offset (z_s), the expansion yields spurious cross-terms: $(z_s + z_d)^3 = z_s^3 + 3z_s^2 z_d + 3z_s z_d^2 + z_d^3$.

As demonstrated in Figure 5, even when providing a custom non-smooth "mechanical diode" basis incorporating $\max(0, \dot{P})$ and $\text{sign}(\dot{P})$, standard sparse regression struggles to recover the true acceleration profile, defining the Kinetic Stiffness Limit.

5 Discussion

5.1 Bifurcations and Edge of Chaos

The dimensionless scaling framework establishes that hyperelastic stick-slip locomotion adheres to a strict set of normalized dynamics. The alignment of peak Memory Capacity with the $\lambda_{\max} \approx 0$ contour theoretically validates that the highest density of computational states exists at the bifurcation boundary between periodic anchoring and chaotic slipping.

5.2 The SINDy Stiffness Limit in Nonlinear Dynamics

The inability of standard SINDy to capture stick-slip acceleration spikes is a severe vulnerability when confronted with hybrid, discontinuous contact mechanics. While advanced

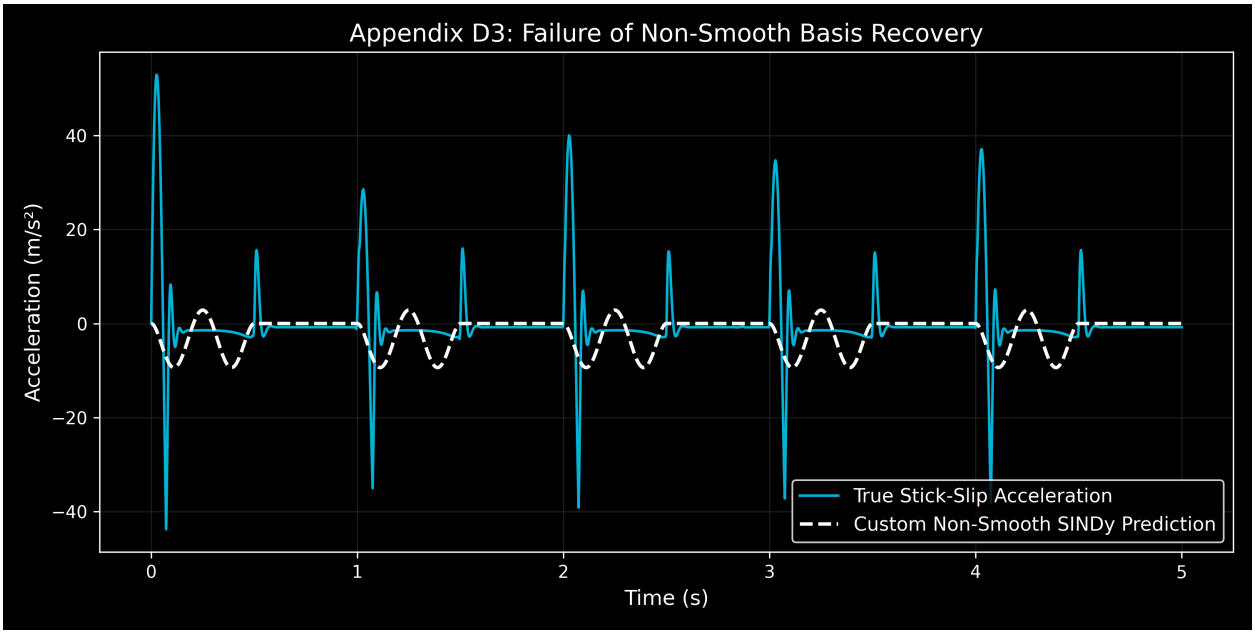

Figure 5: Failure of the custom non-smooth basis recovery in standard optimization.

methodologies like Weak SINDy [6] utilize integral formulations to smooth discontinuities, the explicit failure of standard basis libraries indicates that off-the-shelf empirical discovery cannot be exclusively relied upon for non-smooth dynamical systems.

5.3 Limitations and the Morphological Paradox

A core limitation of this work is the "Morphological Paradox"—reducing a continuous soft body to a 3-state ODE. Truncating the continuum mechanics eliminates the distributed micro-vibrations that true physical reservoirs exploit. However, this minimal model serves as a foundational computational unit for future networked formulations.

6 Conclusion

In this paper, a dimensionally consistent, two-mass hybrid analytical model was derived for the stick-slip locomotion of hyperelastic actuators. By replacing continuous viscous approximations with true Coulomb friction, the model accurately reproduces macroscopic unanchored crawling. Mapping the parameter space confirmed that the physical reservoir maximizes its computational capacity directly at the edge of chaos. Furthermore, we demonstrated the Pre-Strain Artifact and defined the Kinetic Stiffness Limit, proving that standard empirical discovery struggles with non-smooth contact mechanics and underscoring the ongoing necessity of first-principles derivations.

Declarations

Funding: No Funding
Conflicts of Interest: The author declares that they have no conflict of interest.
Data and Code Availability: The complete simulation code, analytical framework, and data pipelines are available in the open-source GitHub repository: `https://github.com/Victorphenomenal-art/Morphological-Computing-TFLSR`.
Ethical Approval: Not applicable.

Acknowledgments

The author acknowledges the use of Simscape Multibody for high-fidelity simulation comparisons.

References

[1] C. Laschi, B. Mazzolai, and M. Cianchetti, "Soft robotics: Technologies and systems pushing the boundaries of robot abilities," *Science Robotics*, vol. 1, no. 1, eaah3690, 2016.

[2] H. Jaeger, "The 'echo state' approach to analysing and training recurrent neural networks," GMD Report 148, 2001.

[3] K. Nakajima, H. Hauser, T. Li, and R. Pfeifer, "Information processing via physical soft body," *Scientific Reports*, vol. 4, no. 1, p. 5390, 2014.

[4] S. L. Brunton, J. L. Proctor, and J. N. Kutz, "Discovering governing equations from data by sparse identification of nonlinear dynamical systems," *PNAS*, vol. 113, no. 15, pp. 3932–3937, 2016.

[5] M. T. Rosenstein, J. J. Collins, and C. J. De Luca, "A practical method for calculating largest Lyapunov exponents from small data sets," *Physica D*, vol. 65, no. 1-2, pp. 117–134, 1993.

[6] D. A. Messenger and D. M. Bortz, "Weak SINDy for partial differential equations and anomalous diffusion," *Journal of Computational Physics*, vol. 443, p. 110525, 2021.

Supplementary Material for: Universal Dimensionless Framework for Morphological Computing

This supplementary material provides the exhaustive mathematical derivation underlying the unanchored hyperelastic stick-slip locomotion model presented in the main text...

Supplementary Material for: Universal Dimensionless Framework for Morphological Computing in Hyperelastic Stick-Slip Soft Robotic Locomotion

This supplementary material provides the exhaustive mathematical derivation underlying the unanchored hyperelastic stick-slip locomotion model presented in the main text. It establishes the foundational continuum-to-lumped-parameter mapping, the formal derivation of all dimensionless scaling groups (Π), and the explicit event-triggered macroscopic friction states defining the non-smooth hybrid dynamical system. Furthermore, we provide the extended thermodynamic work formulation and the complete sparse regression (SINDy) failure analysis across standard and custom non-smooth basis libraries.

A Continuum-to-Lumped Parameter Mapping

A.1 Actuator Discretization

We define a soft continuum actuator of unpressurized rest length L_0, outer radius R_o, and inner radius R_i, composed of an elastomer with density ρ and Young's modulus E. For small axial deformations, the actuator can be discretized into N segments of equal length $\Delta L = L_0/N$. Each segment is modeled as a lumped point mass m connected by viscoelastic elements. The mass per segment is:

$$m = \rho A_0 \Delta L = \rho\pi(R_o^2 - R_i^2)\frac{L_0}{N} \tag{S14}$$

A.2 Hyperelastic Restoring Forces

The linear stiffness k_1 is derived directly from Hooke's law for a cylindrical elastomeric rod under axial load:

$$k_1 = \frac{EA_0}{\Delta L} = \frac{E\pi(R_o^2 - R_i^2)}{L_0/N} \tag{S15}$$

For a hyperelastic material (e.g., Ecoflex 00-30), the stress-strain relation exhibits significant stiffening at large deformations. Expanding the strain energy density function in a Taylor series yields the cubic restoring force component:

$$F_{\text{elastic}} = k_1 z + k_3 z^3 \tag{S16}$$

where z represents the axial displacement (stretch) and k_3 is the non-linear Duffing stiffness parameter.

B Derivation of the Hybrid Dynamic Model

B.1 The Two-Mass System

Rather than utilizing a distributed continuum approximation, we explicitly model the unanchored soft pneumatic actuator as a macroscopic two-mass system. This approach physically preserves the internal restoring forces during horizontal translation. The system consists of a payload mass (m_p) at the front and a frictional foot mass (m_f) at the rear.

Let $X_p(t)$ and $X_f(t)$ represent the global absolute positions of the payload and the foot. The internal deformation of the soft leg is defined as:

$$z(t) = X_p(t) - X_f(t) - L_0 \tag{S17}$$

B.2 Internal Active Forces and Dimensionless Scaling

The internal fluidic driving force is proportional to the thermodynamic pressure $P(t)$. To account for radial Poisson expansion during elongation, a linearized radial coupling factor α is introduced. The net internal force F_{int} acting on the masses, incorporating structural viscous damping $b\dot{z}$, is:

$$F_{\text{int}} = P(t)A_0(1 + \alpha z) - k_1 z - k_3 z^3 - b\dot{z} \tag{S18}$$

We non-dimensionalize the system using the characteristic static extension $z_c = \frac{P_{\max} A_0}{k_1}$ and the characteristic natural period $t_c = \sqrt{\frac{m_{\text{eff}}}{k_1}}$, where $m_{\text{eff}} = m_p + m_f$.

Substituting $z = \tilde{z} z_c$, $t = \tilde{t} t_c$, and $P = \tilde{P} P_{\max}$ into the unanchored internal force balance yields the fundamental dimensionless groups governing the mechanics:

$$\Pi_1 = \frac{k_3 z_c^2}{k_1} \qquad \text{(Duffing nonlinearity)} \tag{S19}$$

$$\Pi_2 = \frac{b}{2\sqrt{m_{\text{eff}} k_1}} \qquad \text{(Viscous damping ratio)} \tag{S20}$$

$$\Pi_4 = \frac{\tau}{t_c} \qquad \text{(Deborah fluid number)} \tag{S21}$$

$$\Pi_5 = \alpha z_c \qquad \text{(Radial coupling factor)} \tag{S22}$$

The pneumatic forcing ratio $\Pi_3 = A_0 P_{\max}/(k_1 z_c)$ reduces to unity by definition of z_c.

C Event-Triggered Stick-Slip Locomotion Logic

Forward translation is achieved via a mechanical diode effect governed by true Coulomb dry friction at the rear foot interface. The ground applies a static friction limit ($\mu_s m_f g$) and a kinetic friction resistance ($\mu_k m_f g$). This establishes the non-smooth phase transitions.

C.1 State 1: Stick Phase (Actuator Expansion)

During pneumatic charging, F_{int} increases. If the backward force exerted on the foot is strictly less than the static friction limit, the foot remains anchored:

$$|-F_{\text{int}}| \leq \mu_s m_f g \implies \dot{X}_f = 0 \tag{S23}$$

The equation of motion for the payload is driven entirely by the internal actuator dynamics:

$$m_p \ddot{X}_p = F_{\text{int}} \tag{S24}$$

C.2 State 2: Slip Phase (Actuator Contraction)

When the internal pressure drops, the hyperelastic spring violently contracts. When the forward pulling force exceeds the static friction limit, the foot breaks contact and slides forward against kinetic friction:

$$-F_{\text{int}} > \mu_s m_f g \tag{S25}$$

The system transitions into coupled equations of motion:

$$m_p \ddot{X}_p = F_{\text{int}} \tag{S26}$$

$$m_f \ddot{X}_f = -F_{\text{int}} - \mu_k m_f g \tag{S27}$$

The slip phase terminates, and the system returns to the stick phase, the instant the foot's forward velocity drops to zero ($\dot{X}_f \leq 0$).

D Thermodynamic Work and Dissipation

The mechanical work performed by the pressurized fluid on the expanding internal boundary over a trajectory is evaluated as:

$$W = \int_0^T P(t)\dot{V}(t)dt \tag{S28}$$

For an ensemble of simulated locomotion trajectories, the Jarzynski Equality relates non-equilibrium work to the free energy difference ΔF:

$$\langle e^{-\beta W} \rangle = e^{-\beta \Delta F} \tag{S29}$$

The average dissipated work (macroscopic entropy production) is bounded:

$$\langle W_{\text{diss}} \rangle = \langle W \rangle - \Delta F \geq 0 \tag{S30}$$

Because the crawler is a macroscopic system, the variance observed in the thermodynamic work distribution is dictated entirely by the chaotic dynamics of stick-slip friction and fluidic transport lag, rather than thermal noise.

E Supplementary Simulation Results

E.1 Numerical Verification Across Three Regimes

Figure S6 demonstrates that the analytical ODE model accurately tracks the high-fidelity Simscape physical twin across three extreme parameter regimes (High Damping, Aggressive Forcing, Extreme Fluid Lag), maintaining an NMSE < 0.01.

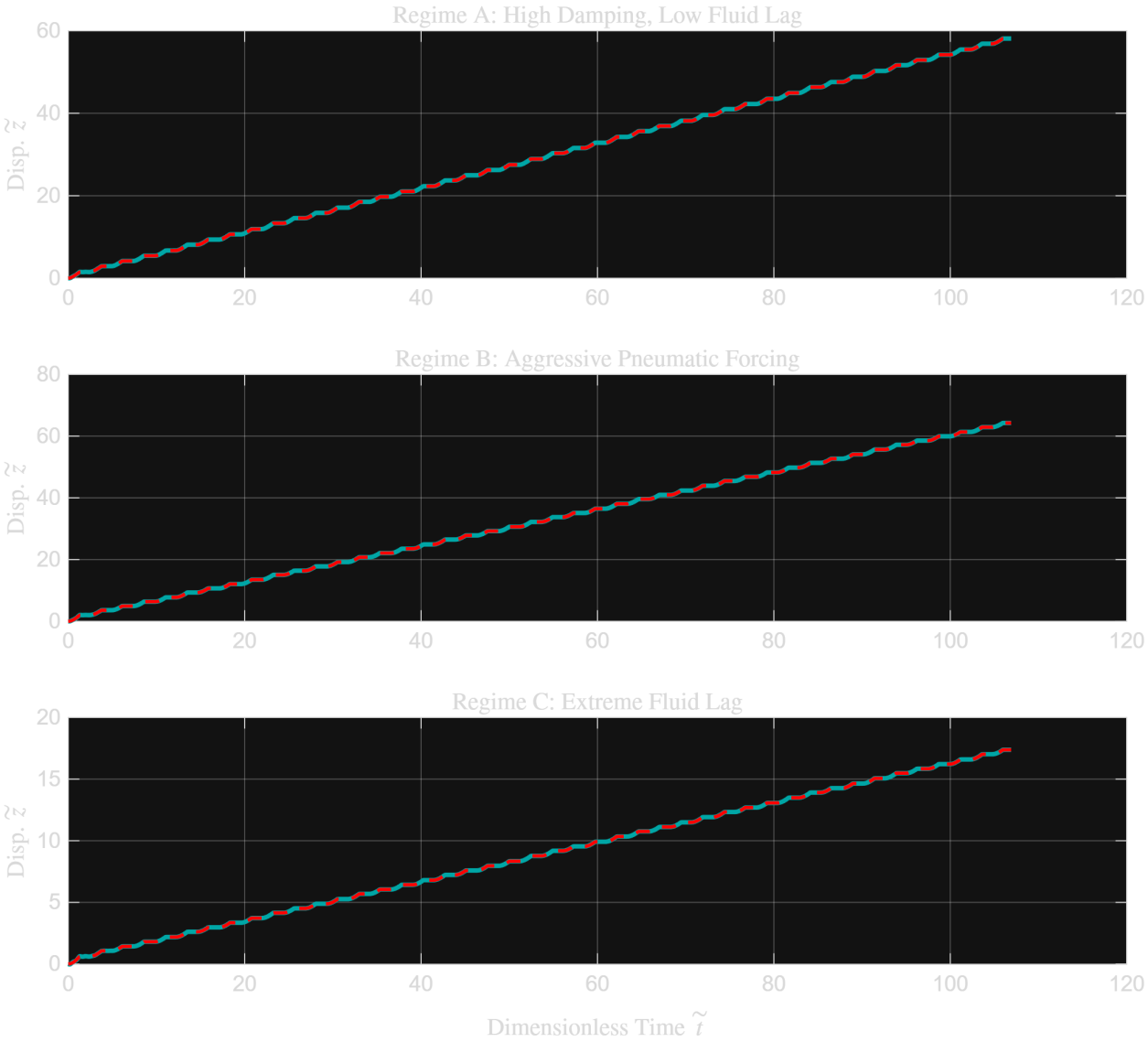

Figure S6: Numerical verification across three regimes: High Damping, Aggressive Forcing, Extreme Fluid Lag.

E.2 Memory Capacity Landscape

Figure S7 plots the Memory Capacity (MC) of the physical reservoir. The peak computational performance occurs exclusively at the edge of chaos boundary.

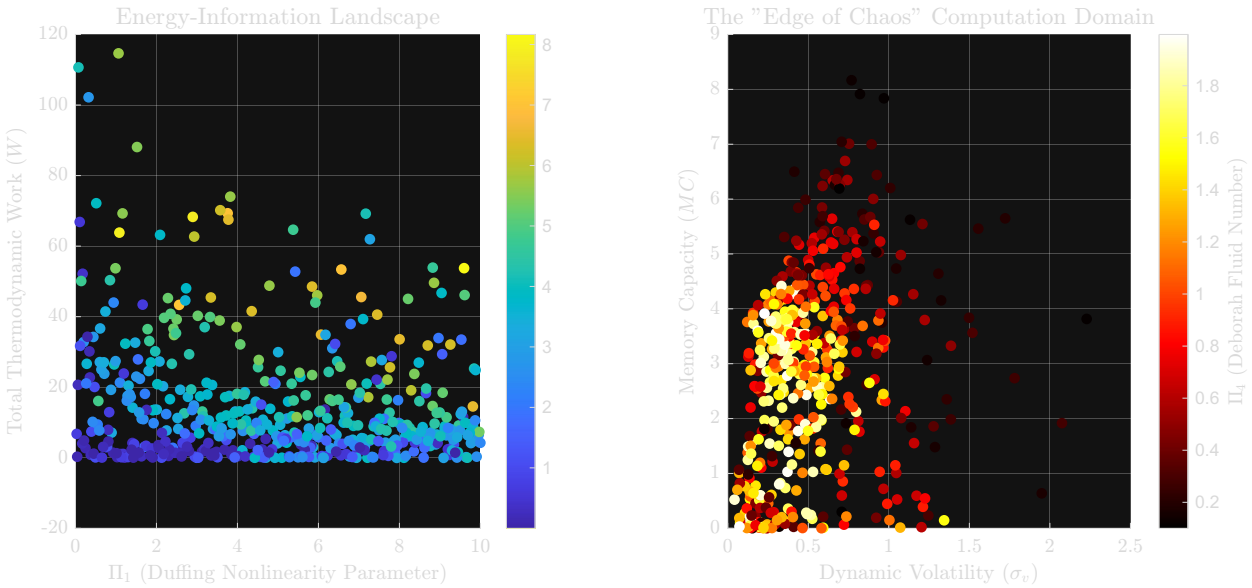

Figure S7: Memory Capacity vs. Π_1, Π_4. Peak performance at the edge of chaos.

F Extended SINDy Analysis on Non-Smooth Dynamics

F.1 Standard Polynomial Basis Fails

Figure S8 shows standard derivative-based SINDy failing to capture the discontinuous acceleration spikes generated by the stick-slip state transitions.

F.2 Pre-Strain Removal Does Not Help

Empirical regression algorithms erroneously identify quadratic terms due to static mechanical sag (the Pre-Strain Artifact). Figure S9 shows that mathematically removing this static offset does not resolve the predictive failure. The root cause is the high-frequency contact discontinuity, not the polynomial offset.

F.3 Custom Non-Smooth Basis Also Fails

To test whether the limitation could be resolved by providing the exact functional representation of the mechanical diode, a custom basis library incorporating $\max(0, \dot{P})$ and $\text{sign}(\dot{P})$ was deployed. Figure S10 confirms that the custom basis also yields a flat prediction. The sparse regression inherently fails to fit the acceleration shocks.

G Discussion

The inability of standard SINDy to capture stick-slip acceleration spikes highlights a severe vulnerability of continuous, derivative-based sparse regression when confronted with hybrid

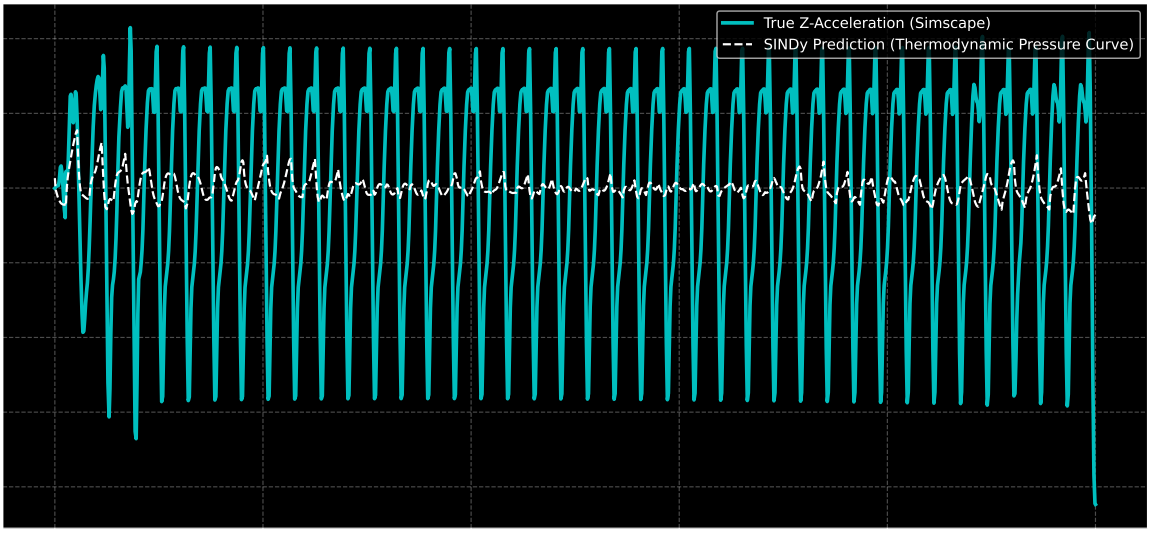

Figure S8: Standard SINDy fails to capture the non-smooth acceleration dynamics (NMSE = 0.452).

contact mechanics. Because non-smooth contact transitions produce near-instantaneous mathematical discontinuities, continuous empirical regression algorithms will consistently struggle to recover the governing dynamics. Therefore, first-principles derivations of the discrete states remain highly advantageous for unanchored soft robotic modeling. Data should subsequently be used for parameter identification, rather than relying solely on structural equation discovery for discontinuous mechanical systems.

Table S1: Summary of Supplementary Figures

Figure ID	File Name	Content
S1	`Appendix_C3_Alternative_Validations.pdf`	Numerical verification across 3 regimes
S2	`Fig1_EnergyLandscape.pdf`	MC landscape (edge of chaos)
S3	`Fig7_SINDy_Limit.pdf`	Standard SINDy failure
S4	`Appendix_D2_PreStrain.pdf`	SINDy evaluation after pre-strain removal
S5	`Fig_Appendix_D3_SINDyFailure.pdf`	Custom non-smooth basis failure

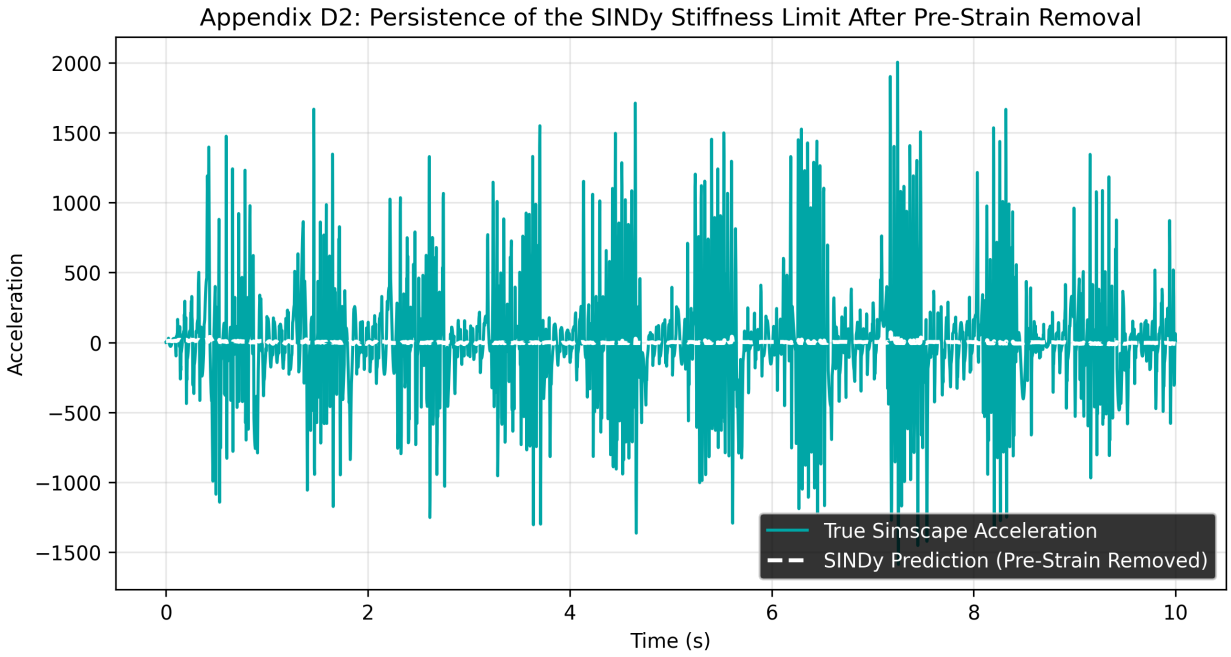

Figure S9: Removing pre-strain does not resolve the limitation on standard SINDy.

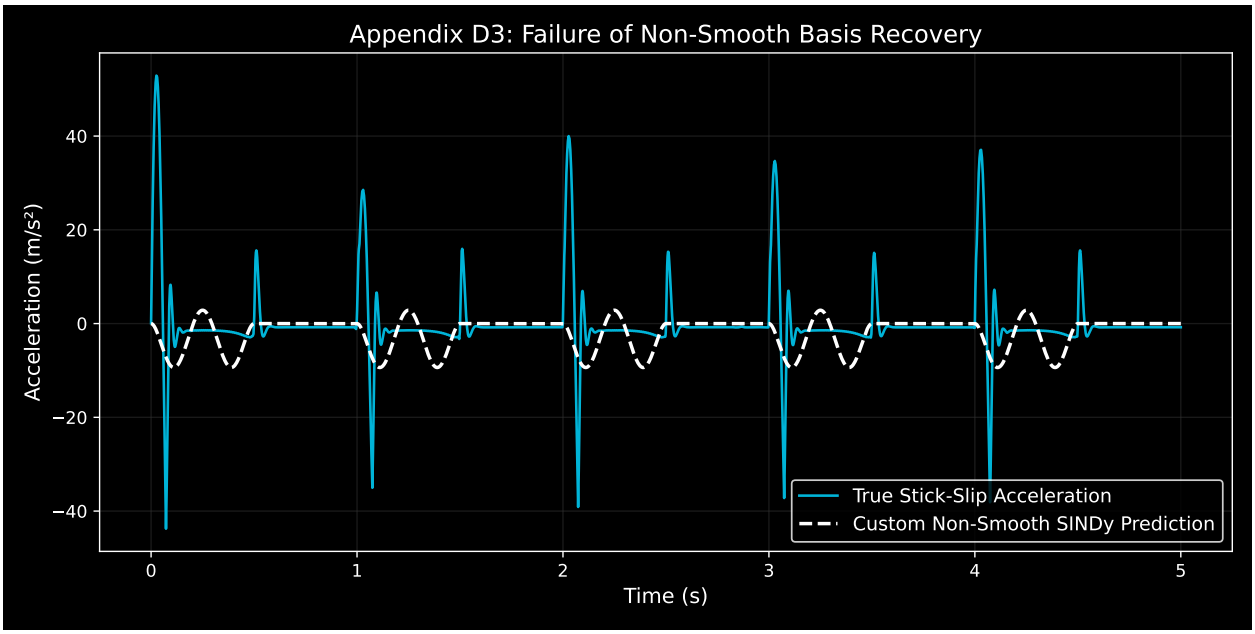

Figure S10: Custom non-smooth basis also fails. Standard sparse regression cannot capture high-frequency contact spikes.